

1 **Microphysical characteristics of precipitation within**
2 **convective overshooting over East China observed by**
3 **GPM DPR and ERA5**

4 Nan Sun¹, Gaopeng Lu¹, Yunfei Fu¹

5 ¹School of Earth and Space Sciences, University of Science and Technology of China, Hefei, 230026,
6 China

7 *Corresponding to:* Yunfei Fu, fyf@ustc.edu.cn

8 **Abstract.** We examine the geographical distribution and microphysical three-dimensional structure of
9 convective overshooting over East China by matching Global Precipitation Measurement
10 Dual-frequency Precipitation Radar instrument (GPM DPR) with European Centre for Medium-Range
11 Weather Forecasts 5th Reanalysis (ERA5). Convective overshooting mainly occur over Northeast China
12 (NC) and northern Middle and East China (MEC) and its frequency varies from 4×10^{-4} to 5.4×10^{-3} .
13 Radar reflectivity of convective overshooting over NC accounts for a higher proportion below the
14 freezing level, while MEC and South China (SC) account for a higher proportion above the freezing level,
15 indicating stronger upward motion and more ice crystal particles. The microphysical processes within
16 convective overshooting are unique, leading to various properties of the droplets in precipitation.
17 Droplets of convective overshooting are large, but sparse, with an effective droplet radius of nearly 2.5
18 mm below 10 km, which is about twice that of non-overshooting precipitation. Findings of this study
19 may have important implications for the microphysical evolution associated with convective
20 overshooting, and provide more accurate precipitation microphysical parameters as input for model
21 simulations.
22

23 **1 Introduction**

24 Convective overshooting provides a rapid transport mechanism that can irreversibly transport water
25 vapor and chemical constituents from lower troposphere to the upper troposphere and lower stratosphere
26 (UTLS) by mixing them with environmental air (Fueglistaler et al., 2004; Frey et al., 2015), which has a
27 direct impact on radiation balance and global climate change (Solomon et al., 2010). As one of the main
28 sources of ozone destroying OH hydroxyl radicals, stratospheric water vapor can help to destroy ozone,
29 which has potential effects on radiative forcing (Anderson et al., 2012). Water vapor enters the
30 stratosphere mainly through the tropical tropopause layer. Several studies show that tropical convective
31 overshooting has a net dehydrating effect on the stratospheric humidity (Danielsen, 1993; Sherwood and
32 Dessler, 2001), while modeling and observational studies have universally show tropical convective
33 overshooting hydrating the stratosphere (Chaboureau et al. 2007; Jensen et al. 2007; De Reus et al. 2009;
34 Avery et al. 2017) because of the injection of ice mass into the stratosphere (Grosvenor et al., 2007; Corti
35 et al., 2008; Chemel et al., 2009; Khaykin et al., 2009). In midlatitude, observations and model
36 simulations show that deep convective overshooting is also an important source for the lower
37 stratospheric water vapor (Liu and Liu, 2016; Smith et al., 2017; Liu et al., 2020; Werner et al., 2020;
38 Wang et al., 2023). Wang et al. (2023) use a high-resolution numerical model to study convective
39 overshooting moistening in the midlatitude lower stratosphere and results show that convective water
40 vapor plumes above 380-K temperature are stable in the stratosphere, while that closer to the
41 tropopause and cloud tops are less stable. In addition to these impacts on water vapor, the effects of
42 convective overshooting on the temperature of the UTLS have also attracted much attention (Sherwood
43 et al., 2003; Chae et al., 2011; Biondi et al., 2012). Given these potentially significant impacts, it is of
44 high importance to understand the characteristics of convective overshooting, which have attracted
45 considerable attention in recent years (Johnston et al., 2018; Muhsin et al., 2018).

46 Perhaps one of the most poorly understood features of convective overshooting is the microphysical
47 structure of precipitation, such as particle size, concentration, phase state and other parameters.
48 Understanding the microphysical characteristics of convective overshooting is helpful to clarify the
49 efficiency of water vapor transport to the lower stratosphere by convective overshooting. And the
50 microphysical processes within convective overshooting are closely related to storm dynamics and
51 thermodynamics through latent heat, and the quantitative description of microphysical characteristics is

52 helpful to improve the accuracy of model simulation parameters (Homeyer and Kumjian, 2015). In
53 addition, thunderstorms with overshooting tops are closely associated with hazardous weather at the
54 Earth's surface, such as heavy rainfall, large hail, damaging winds and tornadoes (Reynolds, 1980;
55 Negri and Adler, 1981; Fujita 1989; Kellenbenz et al., 2007; Brunner et al., 2007; Setvák et al. 2010;
56 Dworak et al. 2012; Line et al., 2016; Bedka et al., 2018; Marion et al., 2019), indicating the application
57 of overshooting detections for severe weather warnings (McCann 1983; Bedka, 2011; Homeyer and
58 Kumjian, 2015). Bedka (2011) have studied relationship between overshooting cloud tops with severe
59 weather over Europe and results show that an overshooting was found near 47% of the confirmed
60 severe weather events. Specifically, overshooting top-severe weather relationship is strong for large
61 hail (53%) and severe wind (52%) but relatively weak for tornado events (14%). Dworak et al. (2012)
62 show that severe weather was often associated with overshooting detections during warm season
63 (April-September). Furthermore, convective overshooting generates gravity waves, and gravity wave
64 breaking generates turbulence, which is of fundamental importance in the generation of small-scale
65 motions that influence aircraft (Lane and Sharman, 2006). Tens of commercial airline passengers are
66 injured each year over the continental United States during turbulence-related aviation incidents (Lane
67 et al., 2003). Cloud-to-ground lightning is also found to occur frequently near convective overshooting
68 region, which is also a threat to aviation safety (Bedka, 2011). In summary, hazardous weather
69 accompanied by convective overshooting have serious harm to social economy and human production
70 and life. Quantitative study of the precipitation structure of convective overshooting can help figure the
71 relationship between convective overshooting and severe weather like heavy rainfall out, providing a
72 predictor for severe weather warning and ensuring aviation safety. Liu et al. (2012) studied the
73 climatological characteristics of convective overshooting and found convective overshooting show
74 remarkable regionality and seasonal variations. Homeyer and Kumjian (2015) observed the radar
75 reflectivity characteristics of convective overshooting from the analysis of the polarimetric radar
76 observations. Although the above studies have explored the characteristics of some precipitation
77 parameters within convective overshooting, we still lack the understanding of more precipitation
78 microphysical parameters and more detailed microphysical processes within convective overshooting
79 due to the limitations of observation methods.

80 To fully study the microphysical characteristics of convective overshooting, accurate methods of
81 detecting the frequency and long-term distribution of convective overshooting are required. The

82 traditional way for detecting convective overshooting from satellite is to find pixels in infrared imagery
83 with brightness temperatures colder than a given temperature threshold (Machado et al. 1998; Rossow
84 and Pearl 2007). Gettelman et al. (2002) have studied the cloud regions colder than the tropopause
85 temperature on infrared images and found that the frequency of tropical convective overshooting is about
86 0.5%. However, it is impossible to guarantee that the low value of infrared brightness temperature
87 represents clouds penetrating the tropopause rather than cirrus or cloud anvil in the upper air due to the
88 lack of vertical structure information of convection. Also, overshoots mix with relatively warm
89 stratosphere air such that cold pixels are often diminish and not a reliable means to identify overshooting.
90 With the launch of Precipitation Radar aboard Tropical Rainfall Measuring Mission (TRMM),
91 three-dimensional structure information of precipitation within the convective overshooting can be
92 provided (Alcala and Dessler, 2002; Liu and Zipser, 2005) and a new method for detecting the
93 convective overshooting is proposed that is to find pixels with rain top height higher than tropopause
94 height (Xian and Fu, 2015; Sun et al., 2021), which improves the accuracy of detecting convective
95 overshooting. Still, TRMM PR can't provide the precipitation microphysical information, which limits
96 our study on the internal microphysical structure within convective overshooting. Besides, TRMM PR
97 can underestimate the height of convective overshooting because of only sensitive to large precipitation
98 particles (sensitivity at ~17 dBZ) (Takahashi and Luo, 2014).

99 As the continuation of TRMM PR, Global Precipitation Measurement (GPM) carrying the first
100 Dual-frequency Precipitation Radar (DPR) launched in February 2014. GPM DPR includes two bands of
101 precipitation radar, which provides excellent opportunities for studying the microphysical structure of
102 precipitation (Sun et al., 2022a). Liu et al. (2016, 2020) have used GPM KuPR and ERA-Interim
103 6-hourly dataset to study climatology and detection of convective overshooting. However, the above
104 studies only use the KuPR data and mainly focus on the geographical distribution; the vertical and
105 microphysical precipitation structure of convective overshooting remains unknown.

106 East China is a densely populated area, an economic concentration area and an important food
107 producing area in China. Affected by the circulation anomalies of the East Asian tropical and subtropical
108 monsoon and their interactions, extreme precipitation events occur frequently over East China. Many
109 scholars have studied the characteristics of precipitation in East China (Zhang et al., 2018; Xu, 2020), but
110 few have studied the characteristics of convective overshooting and its internal precipitation
111 microphysical structure over East China, which can not only help the flood prevention work in summer

112 over East China, but also ensure social economic development to a certain extent. In addition, there are
113 thousands of airlines over East China, carrying hundreds of millions of passengers every year. In view
114 of the impact of convective overshooting on social economic and aviation safety, it's necessary to
115 conduct relevant research on East China. The purpose of this study is to examine the microphysical
116 characteristics of convective overshooting over East China by matching the precipitation data from GPM
117 DPR and meteorological parameters from ERA5. We will focus on the vertical structure of precipitation
118 within convective overshooting and further explore its microphysical structure feature of precipitation.

119 **2 Data and method**

120 **2.1 DPR-based precipitation dataset**

121 GPM DPR include KuPR (Ku band, 13.6 GHz) and KaPR (Ka band, 35.5 GHz), two bands of
122 precipitation radar. KuPR is similar to TRMM PR and has a longer wavelength, which is better at
123 detecting heavy precipitation (the minimum detected precipitation is about 0.5 mm/h). However, KaPR
124 has a shorter wavelength, which is more sensitive to weak precipitation (the minimum detected
125 precipitation is about 0.2 mm/h). Based on the different echo characteristics of Ku band and Ka band, the
126 dual channel inversion algorithm can be used to retrieve Droplet Size Distribution (DSD). Here we use
127 the precipitation datasets are provided by the GPM level 2 product 2ADPR in version 6. The horizontal
128 resolution is 5 km and the vertical resolution is 125m. The precipitation microphysical parameters
129 provided by GPM 2ADPR include droplet concentration ($dB N_0$) and effective radius (D_0).

130 **2.2 ERA5-based meteorological dataset**

131 The meteorological data are from ERA5 reanalysis product, whose name is "ERA5 hourly data on
132 pressure levels from 1940 to present". And the following parameters are used in this paper: temperature,
133 specific humidity, vertical velocity, U-component of wind, and V-component of wind. The time
134 resolution is 1 h and the horizontal resolution is $0.25^\circ \times 0.25^\circ$. Vertical coverage is 1000 hPa to 1hPa
135 and vertical resolution is 37 pressure levels (1000, 975, 950, 925, 900, 875, 850, 825, 800, 775, 750,
136 700, 650, 600, 550, 500, 450, 400, 350, 300, 250, 225, 200, 175, 150, 125, 100, 70, 50, 30, 20, 10, 7, 5,
137 3, 2, 1 hPa).

138 **2.3 Detection method of convective overshooting**

139 Convective overshooting is defined to occur where the storm top height is above the real-time
140 tropopause height in a precipitation pixel. Obtaining correct tropopause height data with high spatial
141 and temporal resolution is the most important and difficult step in convective overshooting detection.
142 On the one hand, the determination of the tropopause is still under debate. At present, the following four
143 definitions of the tropopause are widely adopted throughout the world: Cold point tropopause, thermal
144 tropopause, dynamic tropopause and ozone tropopause. Cold point tropopause is only physically
145 meaningful in the latitude zone 10°S-10°N near the equator (Highwood and Hoskins, 1998;
146 Rodriguez-Franco and Cuevas, 2013). Dynamic tropopause is based on the differing values of potential
147 vorticity in the troposphere and stratosphere, which applies to extratropical areas (Danielsen et al.,
148 1987; Holton et al., 1995). Ozone tropopause is defined based on the ozone sounding profiles, whose
149 disadvantage is that the choice of ozone mixing ratio thresholds varies with region and season (Bethan
150 et al., 1996; Zahn et al., 2004). Therefore, this paper uses the thermal tropopause, which is defined by
151 the World Meteorological Organization (WMO) (WMO, 1957). The thermal tropopause is based on the
152 temperature lapse rate, also known as lapse-rate tropopause. The accurate calculation of the tropopause
153 height based on this definition, on the other hand, depends on the temperature profile data with high
154 spatial and temporal resolution. The latest generation of reanalysis data ERA5 provides hourly estimates
155 of a large number of atmospheric, land and oceanic climate variables, which has attracted much attention
156 due to its much higher spatial and temporal resolution than its predecessor ERA-Interim, especially in the
157 upper troposphere and lower stratosphere (Hoffmann et al. 2019). Sun et al. (2022b) verified the
158 accuracy for the tropopause height calculated from temperature profiles of ERA5 by comparing ERA5
159 with other popular datasets. Based on the above analysis, the process of convective overshooting
160 detection is shown as follows.

161 Firstly, match each pixel of GPM DPR detection with ERA5 grid data by using the principle of the
162 nearest method. The matching time between GPM and ERA5 is 1 h, and the matching range is $0.25^\circ \times$
163 0.25° . Storm top height is obtained from the GPM DPR.

164 Secondly, real-time tropopause height is calculated from the temperature profiles from ERA5
165 according to the definition from the World Meteorological Organization (WMO, 1957). The
166 algorithmic process is shown as follows: Firstly, find X layer whose atmospheric lapse rate is 2 K km^{-1}

167 or less starting from the first layer (near the ground) of the temperature profile, and then judge whether
168 the atmospheric lapse rate does not exceed 2 K km^{-1} between the X level and all higher levels within 2
169 km, if so, the height of X layer is the tropopause height, if not, repeat the above algorithm starting from
170 the X layer until tropopause layer is found.

171 At last, convective overshooting is identified based on the storm top height and tropopause height.

172 **2.4 Study areas**

173 The study areas are marked as black boxes in Fig. 1a and only the land parts are studied because
174 characteristics of vertical structure of precipitation over land and sea are very different, and this study
175 is limited in space and focuses only on the land region. Using years of NCEP/NCAR reanalysis data,
176 Xia (2015) analyzed the climatic feature of temperature and water vapor in China and divided China into
177 different climatic zones. To have a better understanding of precipitation microphysical structure over
178 different regions of East China, we also divided East China into three climatic zones according to its
179 climatic characteristics and previous studies (Xia, 2015; Sun et al., 2022a). From north to south, they are
180 Northeast China (NC, 38° – 50° N, 118° – 130° E), Middle and East China (MEC, 26.5° – 38° N, 112° –
181 123° E), and South China (SC, 18° – 26.5° N, 108° – 123° E). For the three regions, the lower latitude areas
182 have higher surface temperature, greater temperature lapse rate and lower temperature of stratosphere.
183 Temperature profiles of same latitude are essentially same over SC and MEC, and temperature signals
184 exist meridional differences over NC. Atmospheric humidity has remarkable regional characteristics.
185 SC is wetter, with the surface relative humidity of more than 70%, while NC and MEC are drier and
186 their humidity range from 50% to 70% (Xia, 2015). The study time frame is defined as the time from
187 2014 to 2020 in summer (June, July and August)

188 **3 Results**

189 **3.1 Case studies**

190 Three cases selected from NC, MEC and SC are analyzed to lay a foundation for the subsequent
191 statistical analysis. The precipitation characteristics of the three cases are shown as Fig. 2. The Case 1
192 (C1) occurs in NC at 14:00 on July 1, 2017. Convective overshooting is observed in a total of 65 pixels
193 for C1, whose mean rain rate are 20.7 mm/h (Fig. 2a) and mean storm top height are 14.1 km (Fig. 2b).
194 The strong radar reflectivity along A1B1 occurs at 35–95km away from point A1, and the strongest echo

195 is up to 50 dBZ, appears at 0-5 km (Fig. 2c). The maximum echo height is about 15 km, 2 km higher than
196 the tropopause height. The Case 2 (C2) occurs in MEC at 13:00 on July 30, 2015. Convective
197 overshooting is observed in a total of 58 pixels for C2, and their mean rain rate are 29.7 mm/h (Fig. 2d)
198 and mean storm top height are 15.2 km (Fig. 2e). The radar echo along A2B2 is very strong and the
199 strongest echo is up to 50 dBZ, which is about 45-95 km away from point A2 (Fig. 2f). The highest echo
200 can reach to about 17 km altitude. The Case 3 (C3) occurs in SC at 17:00 on June 13, 2015. Convective
201 overshooting is observed in a total of 8 pixels for C3 and their mean rain rate are 46.3 mm/h (Fig. 2g) and
202 mean storm top height are 16.9 km (Fig. 2h). The strongest echo occurs at 60-70 km away from point A3
203 and the highest echo can reach to 17.2 km, about 0.5 km higher than the tropopause height (Fig. 2i).

204 To learn about the characteristics of the large scale circulation for these three cases, we calculate the
205 distribution of Precipitable Water Vapor (PWV), streamlines and Vertical Velocity (VV), and locations
206 of the three cases are shown as the black boxes in Fig. 3. In general, areas in which convective
207 overshooting occur have abundant PWV and strong ascending movement. In C1, The PWV of the region
208 in which convective overshooting occurs is between 50 and 55 mm, which is higher than otherwise (Fig.
209 3a). Upward motion near the convective overshooting is strong, ranging from -0.03 to -0.12 Pa/s,
210 contributing to the occurrence of convective overshooting (Fig. 3b). The PWV of C2 is more abundant
211 than C1, and the PWV of the area in which convective overshooting occurs are between 55 and 60 mm
212 (Fig. 3c). The VV near the convective overshooting is mostly between -0.09 and -0.15 Pa/s (Fig. 3d). In
213 C3, the PWV near the precipitation area and convective overshooting area are the most abundant
214 compared with C1 and C2, whose maximum can exceed 70 mm (Fig. 3e). Upward movement near the
215 precipitation area and convective overshooting area are very strong and the VV are between -0.12 and
216 -0.18 Pa/s, which provide abundant water vapor and dynamic conditions for the occurrence of
217 convective overshooting.

218 **3.2 Statistical results**

219 **3.2.1 Geographical distribution**

220 Firstly, the horizontal distribution characteristics of convective overshooting over East China are
221 analysed by designing a more accurate algorithm for convective overshooting determination. Accurate
222 determination of tropopause height is the first step of the convective overshooting determination
223 algorithm. We first analyze geographical distribution of climatological mean of the tropopause height

224 over East China calculated from ERA5, shown as Fig. 1b. In general, the tropopause height over East
225 China is between 11.6 km and 16.7 km and has an obvious zonal distribution pattern: Tropopause height
226 over SC and southern MEC (18-36 °N) is the highest and has small spatial variabilities, concentrated at
227 ~16.7 km. Over northern MEC (36-38 °N), tropopause height decreases and forms a gradient, which
228 decreases to 16 km. Tropopause height over NC is the lowest and continues to decrease in a gradient
229 pattern from south to north, decreasing to 13 km near central NC (45 °N) and 12 km near northern NC
230 (48 °N). Minimum standard deviation of tropopause height appears in SC, along with central and
231 southern MEC, lower than 0.2 km. From northern MEC to northern NC, the standard deviation first
232 increases and then decreases, reaching a maximum of more than 2 km around 42 °N, and standard
233 deviation over NC is generally above 1 km.

234 Obtaining storm top height from precipitation data is the second step of convective overshooting
235 algorithm. Fig. 4 show geographical distribution of storm top height for total precipitation, convective
236 precipitation and convective overshooting. Total precipitation represent the all pixels with rain rate
237 higher than 0 mm/h detected by GPM DPR, and those pixels whose rain type are “Convective” are
238 defined as convective precipitation. As shown, mean storm top height over East China varies from 4.5
239 km to 8.5 km, while convective storm top height is mainly distributed between 3.5 km and 9 km.
240 Convective storm top height over NC and northern MEC are the highest, with most areas exceeding 6.5
241 km and as we noted above, tropopause height in these two regions are lower (Fig. 1b), it can be inferred
242 that convective overshooting events are more likely to occur. Further analysis of the frequency of
243 convective overshooting in the following text will confirm this point. Compared with NC, convective
244 storm top height over SC and southern MEC is lower, mainly distributed below 6.5 km. Storm top height
245 of convective overshooting ranges from 10 km to 21 km (Fig. 4c), much higher than normal precipitation
246 (total and convective precipitation) and increasing gradually from north to south. Storm top heights of
247 convective overshooting over NC and northern MEC are low, distributed between 10 km and 16 km,
248 which is due to a lower tropopause height (Fig. 1b) allowing convection with lower storm top height to
249 reach the stratosphere. This lowers the mean storm top height of convective overshooting in these
250 regions, while tropopause heights over SC and southern MEC range from 16 km to 21 km (Fig. 1b),
251 allowing only strong convection to reach the stratosphere.

252 The frequency of convective overshooting is defined as the number of convective overshooting events
253 divided by the total observed sample number of GPM DPR. Statistical results indicate that the frequency

254 of the convective overshooting over East China is very low, with a magnitude of only 10^{-3} , varying
255 regionally (Fig. 5). Sample size of convective overshooting over NC is the highest, followed by MEC,
256 and SC is the lowest (Table 1). Convective overshooting over NC and northern MEC, whose frequency
257 range from 4×10^{-4} to 5.4×10^{-3} (Fig. 5), occur more frequently than SC and southern MEC, whose
258 frequency is between 2×10^{-4} and 6×10^{-4} , which is mainly because the former has a lower tropopause
259 height and it's easier for convective overshooting to occur.

260 3.2.2 Vertical structures

261 Based on the reflectivity profiles and the rain-rate profiles provided by the GPM DPR instrument, we
262 studied the vertical structure of precipitation within convective overshooting. Contoured Frequency by
263 Altitude Diagrams (CFADs) analysis of radar reflectivity can effectively indicate the three-dimensional
264 structure characteristics of precipitation, which is therefore applied in a large number of precipitation
265 studies (Yuter and Houze, 1995). Fig. 6 shows CFADs of the DPR radar reflectivity. In general, radar
266 reflectivity within convective overshooting is stronger and its storm top height is higher. And the CFADs
267 analysis also shows regional differences. Radar echo intensity of convective overshooting over NC is the
268 weakest, and the echo near surface is mainly distributed from 25 dBZ to 55 dBZ, with sharp peak near 47
269 dBZ, while the peak of the total precipitation is around 16 dBZ. And the max radar echo top within
270 convective overshooting over NC can reach to 13.5 km, 3.3 km higher than the mean precipitation.
271 Compared with NC, radar reflectivity within convective overshooting over SC and MEC are stronger and
272 their CFADs character is more similar. Their echo top height is ~ 18 km, 6.5 km higher than total
273 precipitation, 4.5 km higher than NC, and their echo near surface concentrated around 30-55 dBZ, while
274 that of total precipitation is between 15 dBZ and 43 dBZ. Besides, Radar reflectivity of convective
275 overshooting over NC accounts for a higher proportion below the freezing level (Altitude where the
276 temperature is 0°C), while MEC and SC account for a higher proportion above the freezing level, which
277 indicate that the upward motion within convective overshooting over MEC and SC are stronger and there
278 are larger.

279 Quantitative analysis of the vertical structure of precipitation within convective overshooting is one of
280 the main issues of interest to this study. Shown as Fig. 7, the rain rate profiles of convective overshooting
281 are provided, and to highlight its unique feature, rain rate profiles of total precipitation and convective
282 precipitation are also given. In general, the rain rate of convective overshooting is much higher,

283 especially below the freezing level (~5 km), 5-10 times that of normal precipitation. This indicates
284 stronger convection and a greater concentration of ice. In addition, differences between three regions are
285 obvious. Rain rate of convective overshooting over NC are about half as high as over MEC and SC,
286 which is consistent with the results of radar echo. At 1 km altitude, rain rate of convective overshooting
287 are 12 mm/h (NC), 22.5 mm/h (MEC), and 23 mm/h (SC) respectively. Below freezing level, the
288 variation of rain rate with altitude is not very obvious, and difference of rain rate between convective
289 overshooting and normal precipitation are ~8 mm over NC and ~20 mm over MEC and SC. Above
290 freezing level, rain rate of convective overshooting clearly decreases with increasing altitude, and rain
291 rates are 6mm/h (NC), 10 mm (MEC) and 6.5mm (SC) at 10 km. However, rain rates of other
292 precipitation are no more than 2 mm/h above 8 km, we therefore suggest that the strong upward flow
293 within convective overshooting brings large amounts of moisture from the lower layer to the upper layer.
294 We conduct the Probability Density Function (PDF) analysis on the Near Surface Rain Rate (NSRR)
295 within convective overshooting, and that of total and convective precipitation are also calculated, shown
296 as Fig. 8. Grade of precipitation are as follows: Light rain: <4.9 mm/12 h, Moderate rain: 5.0-14.9
297 mm/12h, Heavy rain: 15.0-29.9 mm/12h, Torrential rain: 30.0-69.9 mm/12h, Downpour: 70.0-139.9
298 mm/12h, and Heavy downpour: ≥ 140.0 mm/12h (General Administration of Quality Supervision, 2012).
299 The PDF curve of NSRR of convective overshooting is clearly different from normal precipitation, and
300 has regional differences. The peak value of PDF of convective overshooting appears at ~10 mm/h,
301 classified as downpour, while that of normal precipitation appears at ~1 mm/h, classified as moderate
302 rain, which is obviously lower than convective overshooting. And the PDF of peak value of convective
303 overshooting over NC is about 11.5%, while that over MEC and SC are about 6%. Besides, sample size
304 of convective overshooting with precipitation grade of heavy downpour account for 34.0% (NC), 46.7%
305 (MEC) and 34.8% (SC) respectively, 3-10 times than normal precipitation, which remind us to pay
306 special attention to the extreme precipitation events caused by convective overshooting that may cause
307 harm to our production and life.

308 **3.2.3 Microphysical features**

309 GPM center provides particle spectrum from dual-frequency radar. Based on the DSD profiles from
310 2ADPR, we further investigate the microphysical structures of convective overshooting. The Liquid
311 Water Path (LWP) and Ice Water Path (IWP) show the overall water content in the atmospheric column,

312 which is closely associated with microphysical processes within convective overshooting. To quantify
313 the characteristics of LWP and IWP within convective overshooting, the PDF of LWP and IWP of
314 convective overshooting are shown as Fig. 9, and that of convective and total precipitation are also
315 shown for comparison. The LWP and IWP within convective overshooting are the highest, with high
316 value of PDF mainly distributed around 1000 g/m^3 and 5000 g/m^3 respectively, much higher than that of
317 normal precipitation, which are around 100 g/m^3 and 300 g/m^3 , indicating sufficient water vapor inside
318 convective overshooting. And differences of IWP between convective overshooting and normal
319 precipitation are bigger than LWP, suggesting that differences of water vapor above freezing level
320 between them is greater and convective overshooting brings water vapor from bottom of the troposphere
321 to higher layers. Besides, differences of LWP and IWP between three regions are also worth noting: The
322 LWP and IWP over MEC and SC are more similar and higher than NC. Especially, LWP over MEC has
323 a bimodal structure with peaks of 630 and 5000 g/m^3 , which are consistent with the bimodal structure of
324 NSRR PDF curve in Fig. 8. Analysis above in Fig. 1b shows that tropopause height over northern MEC
325 is lower than southern MEC, making it easier for convective overshooting to occur over northern MEC.
326 This indicates that there are two types of convective overshooting events over MEC, weak events with
327 lower storm top height and strong events with higher storm top height, which correspond to the two
328 peaks of LWP PDF curve respectively.

329 We further use DSD parameter profiles, including the effective radius (D_0) and droplet concentration
330 (dBN_0) profiles, to analyze the microphysical characteristics within convective overshooting, shown as
331 Fig. 10. Results show that the microphysical processes within convective overshooting are unique,
332 leading to various properties of the droplets in precipitation. Droplets of convective overshooting are
333 large, but sparse. Influenced by strong updrafts, precipitation particles within convective overshooting
334 continuously collide and grow large enough to fall, therefore, the effective radius of droplets are big,
335 below 10 km altitude, almost exceeding 2.5 mm, which is about twice than that of normal precipitation.
336 However, the droplet concentration within convective overshooting is relatively lower. Differences of
337 microphysical structure between three regions are also worth noting. Convective overshooting events
338 over NC have large, but sparse droplets, while that over SC have small, but dense droplets, and the
339 effective radius and concentration of droplets over MEC are between NC and SC, which is speculated
340 that it's related to the differences of aerosol content and types over three regions. Specifically, at 1 km
341 altitude, the effective radius of droplets over NC is the largest (2.87 mm), followed by MEC (2.7 mm),

342 and SC is the lowest (2.5 mm). As altitude increases, the effective radius of droplets first increase and
343 then decrease, with maximum of 2.93 mm over NC at 2.5 km and sharp peak over MEC (2.85 mm) and
344 SC (2.76 mm) near freezing level, about twice than normal precipitation. The effective radius of droplets
345 for convective overshooting over NC and MEC are lower than 2.5 mm above 10 km and 12 km
346 respectively. It's worth noting that the effective radius of droplets for convective overshooting over SC
347 show an increasing trend above 8 km altitude, which are similar to convective precipitation, and their
348 effective radius of droplets over three regions also show an increasing tend from 9 km to 13 km, which
349 may be related to the strong upward motion inside. When the upward motion is strong, ice particles must
350 grow large enough to fall (Langmuir, 1948). Droplet concentration basically decreases with altitude, and
351 that within convective overshooting is obviously lower than normal precipitation and NC is the lowest,
352 while MEC and SC are higher and similar. Droplet concentration within convective overshooting near
353 ground is the highest, with NC (25.4), MEC (28) and SC (28), while that of normal precipitation is
354 mainly distributed between 32 and 35.

355 **4 Summary and conclusions**

356 The microphysical characteristics of convective overshooting are essential but poorly understood due to
357 the difficulty in accurately detecting the convective overshooting and obtaining microphysical
358 parameters during severe weather events. Based on the microphysical precipitation data from GPM DPR
359 and the meteorological data from ERA5 data, we designed a more accurate algorithm for convective
360 overshooting determination and examine the particle size, concentration, phase state and other
361 parameters of the convective overshooting over East China. The main conclusions are:

362 Firstly, the horizontal distribution characteristics of convective overshooting over East China are
363 analysed by designing a more accurate algorithm for convective overshooting determination. Statistical
364 results indicate that the frequency of the convective overshooting over East China is very low, with a
365 magnitude of only 10^{-3} , with large regional differences. Convective overshooting events occur more
366 frequently over NC and northern MEC, than SC and southern MEC, mainly because of the lower
367 tropopause height of the former and the different underlying surfaces. The mean convective overshooting
368 storm top height mostly ranges from 10 km to 21 km and has obvious regional distribution differences,
369 and convective overshooting storm top height over NC is 5-6 km higher than SC.

370 Based on the reflectivity profiles and the rain-rate profiles provided by the GPM DPR instrument, we
371 studied the vertical structure of precipitation within convective overshooting. The CFADs analysis of the
372 radar reflectivity shows that radar reflectivity within convective overshooting is stronger and its storm
373 top height is higher. The CFADs analysis also shows regional differences. Radar reflectivity of
374 convective overshooting over NC accounts for a higher proportion below the freezing level, while MEC
375 and SC account for a higher proportion above the freezing level, which indicate that the upward motion
376 within convective overshooting over MEC and SC are stronger and there are more ice crystal particles.
377 Rain rate results also show that rain rate within convective overshooting is higher, 5-10 times than that of
378 normal precipitation. Especially, sample number of strong precipitation with grade of precipitation of
379 heavy downpour accounts for 34.0% (NC), 46.7% (MEC), and 34.8% (SC), which remind us to pay
380 special attention to the extreme precipitation events caused by convective overshooting.

381 GPM center provides particle spectrum from dual-frequency radar. Based on the DSD profiles from
382 2ADPR, we further investigated the microphysical structures of convective overshooting. Statistical
383 results show that convective overshooting has unique microphysical characteristics compared with
384 normal precipitation, with obvious regional differences. The LWP and IWP within convective
385 overshooting are abundant, with high values of PDF distributed around 1000 g/m^3 and 5000 g/m^3
386 respectively. Moreover, influenced by strong updrafts, precipitation particles within convective
387 overshooting continuously collide and grow large enough to fall, therefore, the effective radius is big,
388 below 10 km altitude, almost exceeding 2.5 mm, which is about twice than that of normal precipitation.
389 However, the droplet concentration within convective overshooting is relatively lower. Differences of
390 microphysical structure between three regions are also worth noting. The effective radius of droplet over
391 NC is slightly bigger than MEC and SC, while the droplet concentration is lower, which is speculated
392 that it's related to the differences of aerosol content and types over three regions.

393 Quantitative study of the internal microphysical characteristics within convective overshooting has not
394 been documented previously. Findings of this study may have important implications for the
395 microphysical evolution associated with convective overshooting, and provide more accurate
396 precipitation microphysical parameters as the input of the model simulation. This study is the
397 continuation of the previous research (Sun et al., 2021). In the future, we will further explore the impact
398 of aerosol on the internal microphysical characteristics within convective overshooting, and more

399 microphysical parameters with higher spatiotemporal resolution are expected to provide more detailed
400 features.

401 **Data availability.** ERA5 data are taken from
402 <https://www.ecmwf.int/en/forecasts/datasets/reanalysis-datasets/era5>. GPM DPR data are archived at
403 <https://gpm.nasa.gov/data/directory>.

404 **Acknowledgements.** This work was funded by the National Natural Science Foundation of China
405 Project (Grant No. 42230612) and the fellowship of China Postdoctoral Science Foundation (Grant
406 Numbers: 2022M723011).

407 **Author contributions.** Sun N., Lu G.P., and Fu Y.F. framed up this study. All the authors discussed the
408 concepts. Sun N. conducted the data analyses. Sun N. drafted the manuscript and all authors edited the
409 manuscript.

410 **Competing interests.** The authors declare no competing interests.

411 **References**

412 Anderson, J. G., Wilmouth, D. M., Smith, J. B. and Sayres, D. S.: UV dosage levels in summer:
413 Increased risk of ozone loss from convectively injected water vapor, *Science*, 337, 835-839,
414 <https://doi.org/10.1126/science.1222978>, 2012.

415 Avery, M. A., Davis, S. M., Rosenlof, K. H., Ye, H. and Dessler, A. E.: Large anomalies in lower
416 stratospheric water vapour and ice during the 2015–2016 El Niño, *Nature Geoscience*, 10, 405-409,
417 <https://doi.org/10.1038/ngeo2961>, 2017.

418 Alcala, C. M. and Dessler, A. E.: Observations of deep convection in the tropics using the Tropical
419 Rainfall Measuring Mission (TRMM) precipitation radar, *Journal of Geophysical Research:*
420 *Atmospheres*, 107, 4792, <https://doi.org/10.1029/2002JD002457>, 2002.

421 Biondi, R., Randel, W. J., Ho, S. P., Neubert, T. and Syndergaard, S.: Thermal structure of intense
422 convective clouds derived from GPS radio occultations, *Atmospheric Chemistry and Physics*, 12,
423 5309-5318, <https://doi.org/10.5194/acp-12-5309-2012>, 2012.

424 Bedka, K., Murillo, E. M., Homeyer, C. R., Scarino, B. and Mersiovsky, H.: The above-anvil cirrus
425 plume: An important severe weather indicator in visible and infrared satellite imagery, *Weather and*
426 *Forecasting*, 33, 1159-1181, <https://doi.org/10.1175/WAF-D-18-0040.1>, 2018.

427 Bethan, S., Vaughan, G., and Reid, S. J.: A comparison of ozone and thermal tropopause heights and the
428 impact of tropopause definition on quantifying the ozone content of the troposphere, *Quarterly*
429 *Journal of the Royal Meteorological Society*, 122(532), 929-944,
430 <https://doi.org/10.1002/qj.49712253207>, 1996.

431 Brunner, J. C., Ackerman, S. A., Bachmeier, A. S. and Rabin, R. M.: A quantitative analysis of the
432 enhanced-V feature in relation to severe weather, *Weather and Forecasting*, 22, 853-872,
433 <https://doi.org/10.1175/WAF1022.1>, 2007.

434 Bedka, K. M.: Overshooting cloud top detections using MSG SEVIRI Infrared brightness temperatures
435 and their relationship to severe weather over Europe, *Atmospheric Research*, 99, 175-189,
436 <https://doi.org/10.1016/j.atmosres.2010.10.001>, 2011.

437 Chaboureaud, J. P., Cammas, J. P., Duron, J., Mascart, P. J., Sitnikov, N. M. and Voessing, H. J.: A
438 numerical study of tropical cross-tropopause transport by convective overshoots, *Atmospheric*
439 *Chemistry and Physics*, 7, 1731-1740, <https://doi.org/10.5194/acp-7-1731-2007>, 2007.

440 Corti, T., Luo, B. P. and De Reus, M. et al.: Unprecedented evidence for deep convection hydrating the
441 tropical stratosphere, *Geophysical Research Letters*, 35, L10810,
442 <https://doi.org/10.1029/2008GL033641>, 2008.

443 Chemel, C., Russo, M. R., Pyle, J. A., Sokhi, R. S. and Schiller, C.: Quantifying the imprint of a severe
444 hector thunderstorm during ACTIVE/SCOUT-O3 onto the water content in the upper
445 troposphere/lower stratosphere, *Monthly weather review*, 137, 2493-2514,
446 <https://doi.org/10.1175/2008MWR2666.1>, 2009.

447 Chae, J. H., Wu, D. L., Read, W. G. and Sherwood, S. C.: The role of tropical deep convective clouds on
448 temperature, water vapor, and dehydration in the tropical tropopause layer (TTL), *Atmospheric*
449 *Chemistry and Physics*, 11, 3811-3821, <https://doi.org/10.5194/acp-11-3811-2011>, 2011.

450 Danielsen, E. F.: In situ evidence of rapid, vertical, irreversible transport of lower tropospheric air into
451 the lower tropical stratosphere by convective cloud turrets and by larger - scale upwelling in tropical
452 cyclones, *Journal of Geophysical Research: Atmospheres*, 98, 8665-8681,
453 <https://doi.org/10.1029/92JD02954>, 1993.

454 De Reus, M., Borrmann, S. and Bansemmer, A. et al: Evidence for ice particles in the tropical stratosphere
455 from in-situ measurements, *Atmospheric Chemistry and Physics*, 9, 6775-6792,
456 <https://doi.org/10.5194/acp-9-6775-2009>, 2009.

457 Danielsen, E. F., Hipskind, R. S. and Gaines, S. E. et al.: Three-dimensional analysis of potential
458 vorticity associated with tropopause folds and observed variations of ozone and carbon monoxide,
459 Journal of Geophysical Research: Atmospheres, 92(D2), 2103-2111,
460 <https://doi.org/10.1029/JD092iD02p02103>, 1987.

461 Dworak, R., Bedka, K., Brunner, J. and Feltz, W.: Comparison between GOES-12 overshooting-top
462 detections, WSR-88D radar reflectivity, and severe storm reports, Weather and Forecasting, 27,
463 684-699, <https://doi.org/10.1175/WAF-D-11-00070.1>, 2012.

464 Fueglistaler, S., Wernli, H. and Peter, T.: Tropical troposphere - to - stratosphere transport inferred from
465 trajectory calculations, Journal of Geophysical Research: Atmospheres, 109, D03108,
466 <https://doi.org/10.1029/2003JD004069>, 2004.

467 Fujita, T. T.: The Teton-Yellowstone tornado of 21 July 1987, Monthly Weather Review, 117,
468 1913-1940, [https://doi.org/10.1175/1520-0493\(1989\)117<1913:TTYTOJ>2.0.CO;2](https://doi.org/10.1175/1520-0493(1989)117<1913:TTYTOJ>2.0.CO;2), 1989.

469 Frey, W., Schofield, R. and Hoor, P. et al.: The impact of overshooting deep convection on local
470 transport and mixing in the tropical upper troposphere/lower stratosphere (UTLS), Atmospheric
471 Chemistry and Physics, 15, 6467-6486, <https://doi.org/10.5194/acp-15-6467-2015>, 2015.

472 General Administration of Quality Supervision, Inspection and Quarantine of the People's Republic of
473 China: Standardization Administration of the People's Republic of China, GB/T 28592—2012 Grade
474 of precipitation, Standards Press of China, 2012.

475 Grosvenor, D. P., Choulaton, T. W., Coe, H. and Held, G.: A study of the effect of overshooting deep
476 convection on the water content of the TTL and lower stratosphere from Cloud Resolving Model
477 simulations, Atmospheric Chemistry and Physics, 7, 4977-5002,
478 <https://doi.org/10.5194/acp-7-4977-2007>, 2007.

479 Gettelman, A., Salby, M. L. and Sassi, F.: Distribution and influence of convection in the tropical
480 tropopause region, Journal of Geophysical Research: Atmospheres, 107, 4080,
481 <https://doi.org/10.1029/2001JD001048>, 2002.

482 Homeyer, C. R. and Kumjian, M. R.: Microphysical characteristics of overshooting convection from
483 polarimetric radar observations, Journal of the Atmospheric Sciences, 72, 870-891,
484 <https://doi.org/10.1175/JAS-D-13-0388.1>, 2015.

485 Hoffmann, L., Günther, G. and Li, D. et al.: From ERA-Interim to ERA5: the considerable impact of
486 ECMWF's next-generation reanalysis on Lagrangian transport simulations, *Atmospheric Chemistry
487 and Physics*, 19, 3097-3124, <https://doi.org/10.5194/acp-19-3097-2019>, 2019.

488 Highwood, E. J. and Hoskins, B. J.: The tropical tropopause, *Quarterly Journal of the Royal
489 Meteorological Society*, 124, 1579-1604, <https://doi.org/10.1002/qj.49712454911>, 1998.

490 Holton, J. R., Haynes, P. H. and McIntyre, M. E. et al.: Stratosphere-troposphere exchange. *Reviews of
491 geophysics*, 33(4), 403-439, <https://doi.org/10.1029/95RG02097>, 1995.

492 Jensen, E. J., Ackerman, A. S. and Smith, J. A.: Can overshooting convection dehydrate the tropical
493 tropopause layer?, *Journal of Geophysical Research: Atmospheres*, 112, D11209,
494 <https://doi.org/10.1029/2006JD007943>, 2007.

495 Johnston, B. R., Xie, F. and Liu, C.: The effects of deep convection on regional temperature structure in
496 the tropical upper troposphere and lower stratosphere, *Journal of Geophysical Research:
497 Atmospheres*, 123, 1585-1603, <https://doi.org/10.1002/2017JD027120>, 2018.

498 Khaykin, S., Pommereau, J. P. and Korshunov, L. et al.: Hydration of the lower stratosphere by ice
499 crystal geysers over land convective systems, *Atmospheric Chemistry and Physics*, 9, 2275-2287,
500 <https://doi.org/10.5194/acp-9-2275-2009>, 2009.

501 Kellenbenz, D. J., Grafenauer, T. J. and Davies, J. M.: The North Dakota tornadic supercells of 18 July
502 2004: Issues concerning high LCL heights and evapotranspiration, *Weather and forecasting*, 22,
503 1200-1213, <https://doi.org/10.1175/2007WAF2006109.1>, 2007.

504 Langmuir, I.: The production of rain by a chain reaction in cumulus clouds at temperatures above
505 freezing, *Journal of the Atmospheric Sciences*, 5(5), 175-192,
506 [https://doi.org/10.1175/1520-0469\(1948\)005<0175:TPORBA>2.0.CO;2](https://doi.org/10.1175/1520-0469(1948)005<0175:TPORBA>2.0.CO;2), 1948.

507 Lane, T. P. and Sharman, R. D.: Gravity wave breaking, secondary wave generation, and mixing above
508 deep convection in a three - dimensional cloud model, *Geophysical Research Letters*, 33,
509 <https://doi.org/10.1029/2006GL027988>, 2006.

510 Lane, T. P., Sharman, R. D., Clark, T. L. and Hsu, H. M.: An investigation of turbulence generation
511 mechanisms above deep convection, *Journal of the atmospheric sciences*, 60, 1297-1321,
512 [https://doi.org/10.1175/1520-0469\(2003\)60<1297:AIOTGM>2.0.CO;2](https://doi.org/10.1175/1520-0469(2003)60<1297:AIOTGM>2.0.CO;2), 2003.

513 Liu, N. and Liu, C.: Global distribution of deep convection reaching tropopause in 1 year GPM
514 observations, *Journal of Geophysical Research: Atmospheres*, 121, 3824-3842,
515 <https://doi.org/10.1002/2015JD024430>, 2016.

516 Liu, N., Liu, C. and Hayden, L.: Climatology and detection of overshooting convection from 4 years of
517 GPM precipitation radar and passive microwave observations, *Journal of Geophysical Research:*
518 *Atmospheres*, 125, e2019JD032003, <https://doi.org/10.1029/2019JD032003>, 2020.

519 Liu, C. and Zipser, E. J.: Global distribution of convection penetrating the tropical tropopause, *Journal of*
520 *Geophysical Research: Atmospheres*, 110, D23104, <https://doi.org/10.1029/2005JD006063>, 2005.

521 Liu, P., Wang, Y., Feng, S., Li, C. Y. and Fu, Y. F.: Climatological characteristics of overshooting
522 convective precipitation in summer and winter over the tropical and subtropical regions, *Chin. J.*
523 *Atmos. Sci.*, 36, 579-589, <https://doi.org/10.3878/j.issn.1006-9895.2011.11109>, 2012.

524 Line, W. E., Schmit, T. J., Lindsey, D. T. and Goodman, S. J.: Use of geostationary super rapid scan
525 satellite imagery by the Storm Prediction Center, *Weather and Forecasting*, 31, 483-494,
526 <https://doi.org/10.1175/WAF-D-15-0135.1>, 2016.

527 Machado, L. A. T., Rossow, W. B., Guedes, R. L. and Walker, A. W.: Life cycle variations of mesoscale
528 convective systems over the Americas, *Monthly Weather Review*, 126, 1630-1654,
529 [https://doi.org/10.1175/1520-0493\(1998\)126<1630:LCVOMC>2.0.CO;2](https://doi.org/10.1175/1520-0493(1998)126<1630:LCVOMC>2.0.CO;2), 1998.

530 Muhsin, M., Sunilkumar, S. V., Ratnam, M. V., Parameswaran, K., Murthy, B. K. and Emmanuel, M.:
531 Effect of convection on the thermal structure of the troposphere and lower stratosphere including the
532 tropical tropopause layer in the South Asian monsoon region, *Journal of Atmospheric and*
533 *Solar-Terrestrial Physics*, 169, 52-65, <https://doi.org/10.1016/j.jastp.2018.01.016>, 2018.

534 Marion, G. R., Trapp, R. J. and Nesbitt, S. W.: Using overshooting top area to discriminate potential for
535 large, intense tornadoes, *Geophysical Research Letters*, 46, 12520-12526,
536 <https://doi.org/10.1029/2019GL084099>, 2019.

537 McCann, D. W.: The enhanced-V: A satellite observable severe storm signature, *Monthly Weather*
538 *Review*, 111, 887-894, [https://doi.org/10.1175/1520-0493\(1983\)111<0887:TEVASO>2.0.CO;2](https://doi.org/10.1175/1520-0493(1983)111<0887:TEVASO>2.0.CO;2),
539 1983.

540 Negri, A. J. and Adler, R. F.: Relation of satellite-based thunderstorm intensity to radar-estimated
541 rainfall, *Journal of Applied Meteorology and Climatology*, 20, 288-300,
542 [https://doi.org/10.1175/1520-0450\(1981\)020<0288:ROSBTI>2.0.CO;2](https://doi.org/10.1175/1520-0450(1981)020<0288:ROSBTI>2.0.CO;2), 1981.

543 Reynolds, D. W.: Observations of damaging hailstorms from geosynchronous satellite digital
544 data, *Monthly Weather Review*, 108, 337-348,
545 [https://doi.org/10.1175/1520-0493\(1980\)108<0337:OODHFG>2.0.CO;2](https://doi.org/10.1175/1520-0493(1980)108<0337:OODHFG>2.0.CO;2), 1980.

546 Rodriguez - Franco, J. J. and Cuevas, E.: Characteristics of the subtropical tropopause region based on
547 long - term highly resolved sonde records over Tenerife, *Journal of Geophysical Research:*
548 *Atmospheres*, 118, 10-754, <https://doi.org/10.1002/jgrd.50839>, 2013.

549 Rossow, W. B. and Pearl, C.: 22 - year survey of tropical convection penetrating into the lower
550 stratosphere, *Geophysical research letters*, 34, L04803, <https://doi.org/10.1029/2006GL028635>,
551 2007.

552 Setvák, M., Lindsey, D. T. and Novák, P. et al.: Satellite-observed cold-ring-shaped features atop deep
553 convective clouds, *Atmospheric Research*, 97, 80-96, <https://doi.org/10.1016/j.atmosres.2010.03.009>,
554 2010.

555 Solomon, S., Rosenlof, K. H. and Portmann, R. W. et al.: Contributions of stratospheric water vapor to
556 decadal changes in the rate of global warming, *Science*, 327, 1219-1223,
557 <https://doi.org/10.1126/science.1182488>, 2010.

558 Sherwood, S. C. and Dessler, A. E.: A model for transport across the tropical tropopause, *Journal of the*
559 *Atmospheric Sciences*, 58, 765-779,
560 [https://doi.org/10.1175/1520-0469\(2001\)058<0765:AMFTAT>2.0.CO;2](https://doi.org/10.1175/1520-0469(2001)058<0765:AMFTAT>2.0.CO;2), 2001.

561 Smith, J. B., Wilmouth, D. M., and Bedka, K. M. et al.: A case study of convectively sourced water
562 vapor observed in the overworld stratosphere over the United States, *Journal of Geophysical*
563 *Research: Atmospheres*, 122(17), 9529-9554, <https://doi.org/10.1002/2017JD026831>, 2017.

564 Sun, N., Fu, Y., Zhong, L., Zhao, C. and Li, R.: The Impact of Convective Overshooting on the Thermal
565 Structure over the Tibetan Plateau in Summer Based on TRMM, COSMIC, Radiosonde, and
566 Reanalysis Data, *Journal of Climate*, 34, 8047-8063, <https://doi.org/10.1175/JCLI-D-20-0849.1>,
567 2021.

568 Sun, N., Fu, Y., Zhong, L. and Li, R.: Aerosol effects on the vertical structure of precipitation in East
569 China, *npj Climate and Atmospheric Science*, 5, 60, <https://doi.org/10.1038/s41612-022-00284-0>,
570 2022a.

571 Sun, N., Zhong, L., Zhao, C., Ma, M. and Fu, Y.: Temperature, water vapor and tropopause
572 characteristics over the Tibetan Plateau in summer based on the COSMIC, ERA-5 and IGRA datasets,
573 Atmospheric Research, 266, 105955, <https://doi.org/10.1016/j.atmosres.2021.105955>, 2022b.

574 Sherwood, S. C., Horinouchi, T. and Zeleznik, H. A.: Convective impact on temperatures observed near
575 the tropical tropopause, Journal of Atmospheric Sciences, 60, 1847-1856,
576 [https://doi.org/10.1175/1520-0469\(2003\)060<1847:CIOTON>2.0.CO;2](https://doi.org/10.1175/1520-0469(2003)060<1847:CIOTON>2.0.CO;2), 2003.

577 Takahashi, H. and Luo, Z. J.: Characterizing tropical overshooting deep convection from joint analysis of
578 CloudSat and geostationary satellite observations, Journal of Geophysical Research: Atmospheres,
579 119, 112-121, <https://doi.org/10.1002/2013JD020972>, 2014.

580 Wang, X., Huang, Y., and Qu, Z. et al.: Convectively Transported Water Vapor Plumes in the
581 Midlatitude Lower Stratosphere, Journal of Geophysical Research: Atmospheres, 128(4),
582 e2022JD037699, <https://doi.org/10.1029/2022JD037699>, 2023.

583 Werner, F., Schwartz, M. J., and Livesey, N. J. et al.: Extreme outliers in lower stratospheric water
584 vapor over North America observed by MLS: Relation to overshooting convection diagnosed from
585 colocated Aqua - MODIS data, Geophysical Research Letters, 47(24), e2020GL090131,
586 <https://doi.org/10.1029/2020GL090131>, 2020.

587 World Meteorological Organization: Meteorology—A three - dimensional science: Second session of
588 the commission for aerology, WMO Bull, 4, 134-138, 1957.

589 Xia, J.: Research on climatic regionalization of China and characteristics of temperature, humidity and
590 wind in precipitation cloud, University of Science and Technology of China, 2015.

591 Xian, T. and Fu, Y.: Characteristics of tropopause - penetrating convection determined by TRMM and
592 COSMIC GPS radio occultation measurements, Journal of Geophysical Research: Atmospheres,
593 120, 7006-7024, <https://doi.org/10.1002/2014JD022633>, 2015.

594 Xu, W.: Thunderstorm climatologies and their relationships to total and extreme precipitation in China,
595 Journal of Geophysical Research: Atmospheres: 125, e2020JD033152,
596 <https://doi.org/10.1029/2020JD033152>, 2020.

597 Yuter, S. E. and Houze, R. A.: Three-dimensional kinematic and microphysical evolution of Florida
598 cumulonimbus. Part II: Frequency distributions of vertical velocity, reflectivity, and differential
599 reflectivity, Monthly Weather Review, 123(7), 1941-1963,
600 [https://doi.org/10.1175/1520-0493\(1995\)123<1941:TDKAME>2.0.CO;2](https://doi.org/10.1175/1520-0493(1995)123<1941:TDKAME>2.0.CO;2), 1995.

601 Zhang, A. and Fu, Y.: Life cycle effects on the vertical structure of precipitation in East China measured
602 by Himawari-8 and GPM DPR, *Monthly Weather Review*, 146, 2183-2199,
603 <https://doi.org/10.1175/MWR-D-18-0085.1>, 2018.

604 Zahn, A., Brenninkmeijer, C. A. M., and Van Velthoven, P. F. J.: Passenger aircraft project CARIBIC
605 1997–2002, Part I: the extratropical chemical tropopause, *Atmospheric Chemistry and Physics*
606 *Discussions*, 4(1), 1091-1117, <https://doi.org/10.5194/acpd-4-1091-2004>, 2004.

607

608 **Tables**

609 **Table1.** The sample number of total precipitation, convective precipitation, and convective overshooting over NC,
610 MEC, and SC.

611

Sample number (count, ct)	NC	MEC	SC
Total Precipitation	652489	546313	319127
Convective Precipitation	111903	137674	111900
Convective Overshooting	2394	582	296

612

613

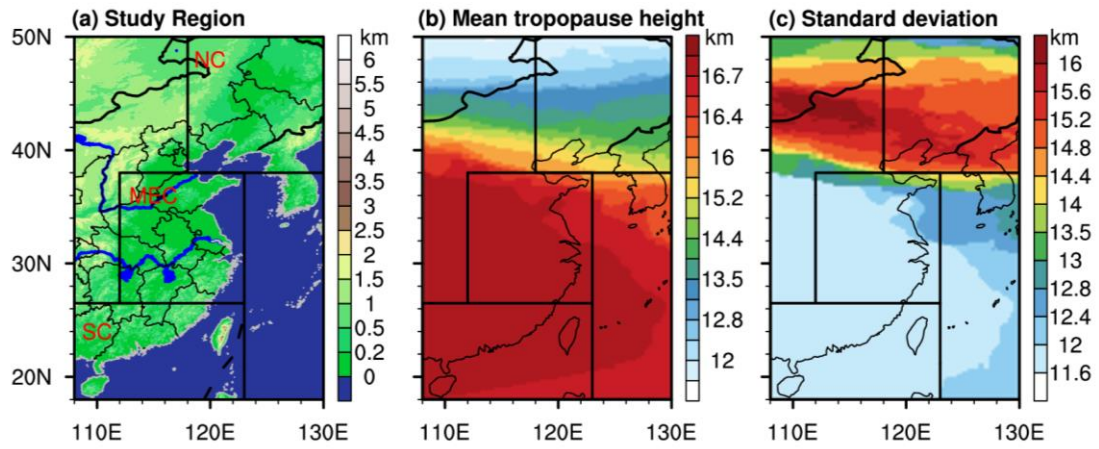
614

615

616

617 **Figures**

618



619

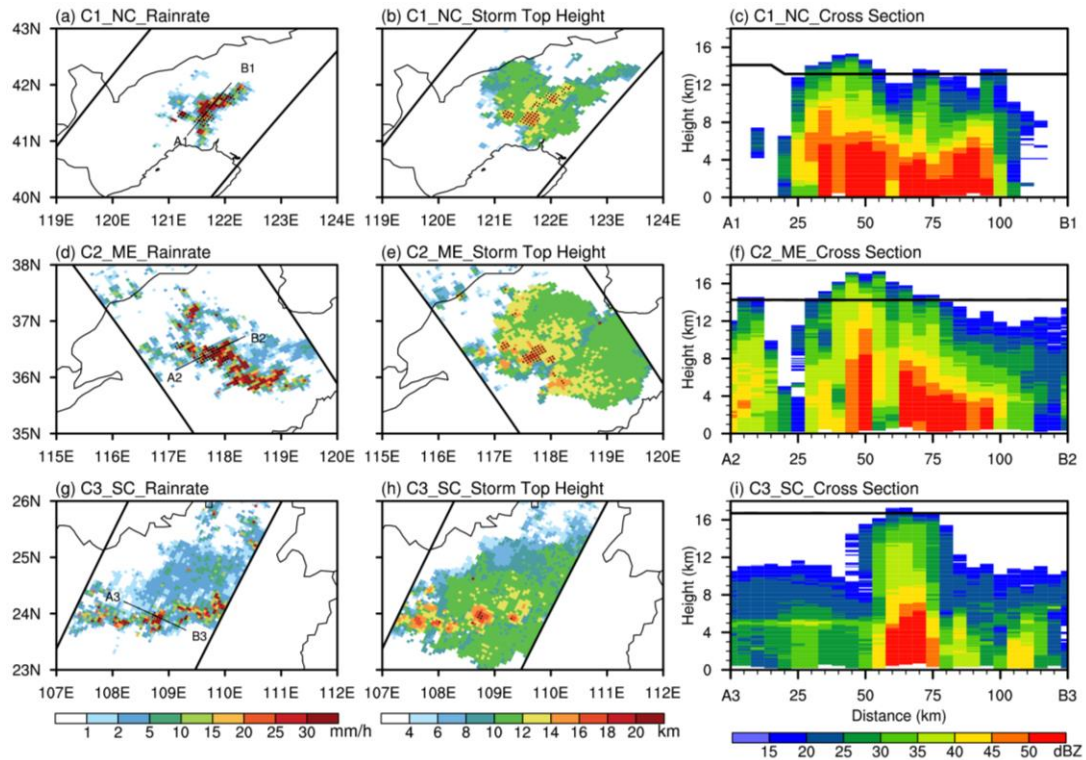
620 **Figure 1.** Study areas and their tropopause characteristics. (a) Regionalization of East China (Black boxes:

621 Divisions between NC, MEC and SC, and only the land surface is studied) and their terrain features. (b)

622 Climatological mean of tropopause height from 2014 to 2020 in summer (June, July and August). (c) Distribution

623 of standard deviation of tropopause height.

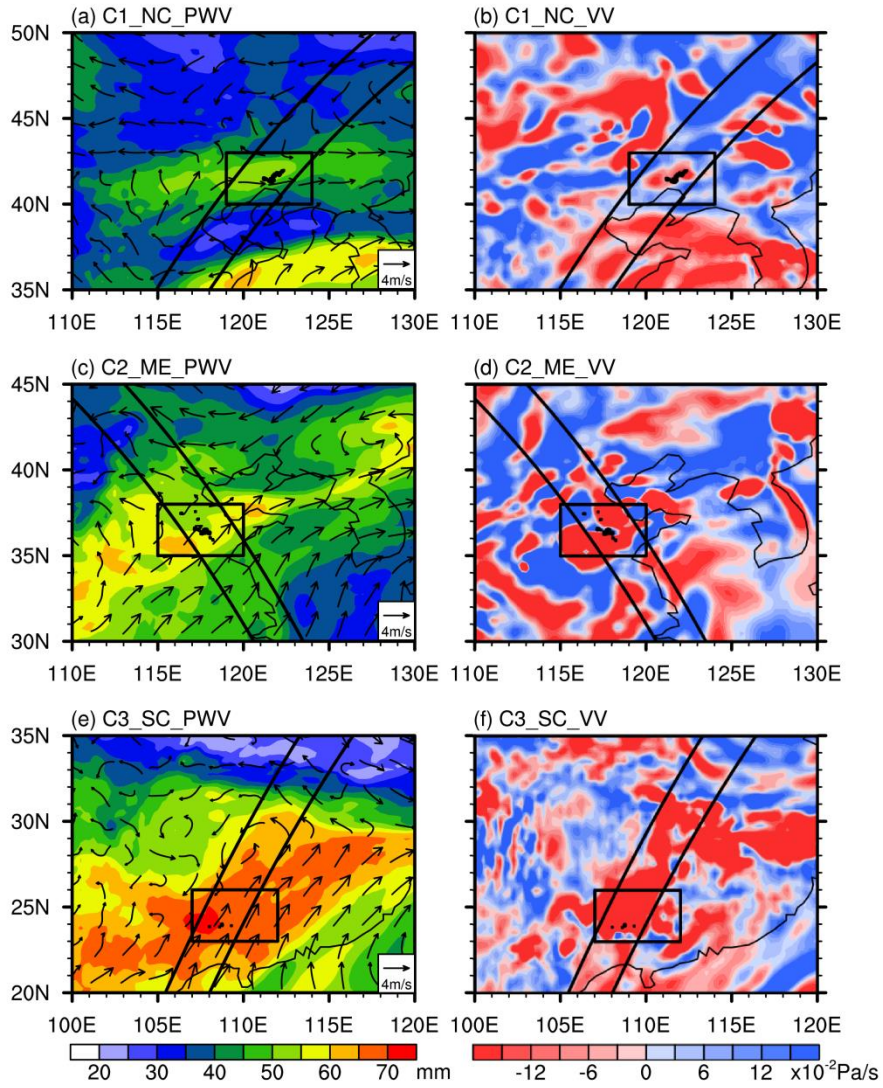
624



625

626 **Figure 2.** Precipitation characteristics of convective overshooting cases. **(a)** Distribution of rain rate of Case 1 (C1).
 627 (The pixels in which convective overshooting occurs are marked as black points). **(b)** Distribution of storm top
 628 height of C1. **(c)** Radar reflectivity cross section along A1B1 and the black line show the tropopause height along
 629 A1B1. **(d)** Distribution of rain rate of C2. **(e)** Distribution of storm top height of C2. **(f)** Radar reflectivity cross
 630 section along A2B2. **(g)** Distribution of rain rate of C3. **(h)** Distribution of storm top height of C3. **(i)** Radar
 631 reflectivity cross section along A3B3.

632

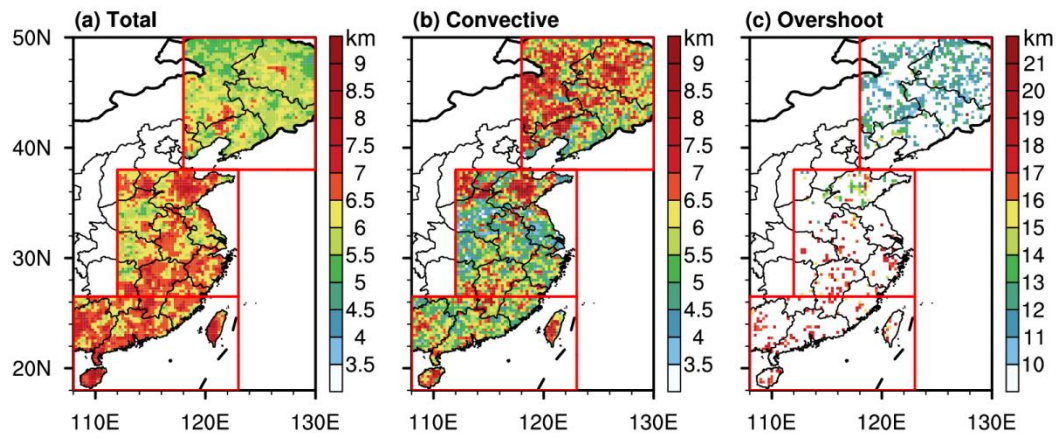


633

634

Figure 3. Characteristics of large scale circulation of convective overshooting cases. **(a)** Distribution of precipitable water vapor (PWV) and streamlines at 850 hPa of C1. The area where the case occurred is marked as big black boxes and the pixels in which convective overshooting occurs are marked as little black boxes. The black line is the GPM detection orbit. **(b)** Distribution of vertical velocity (VV) at 500 hPa of C1. **(c)** Distribution of PWV and streamlines of C2. **(d)** Distribution of VV of C2. **(e)** Distribution of PWV and streamlines of C3. **(f)** Distribution of VV of C3.

640



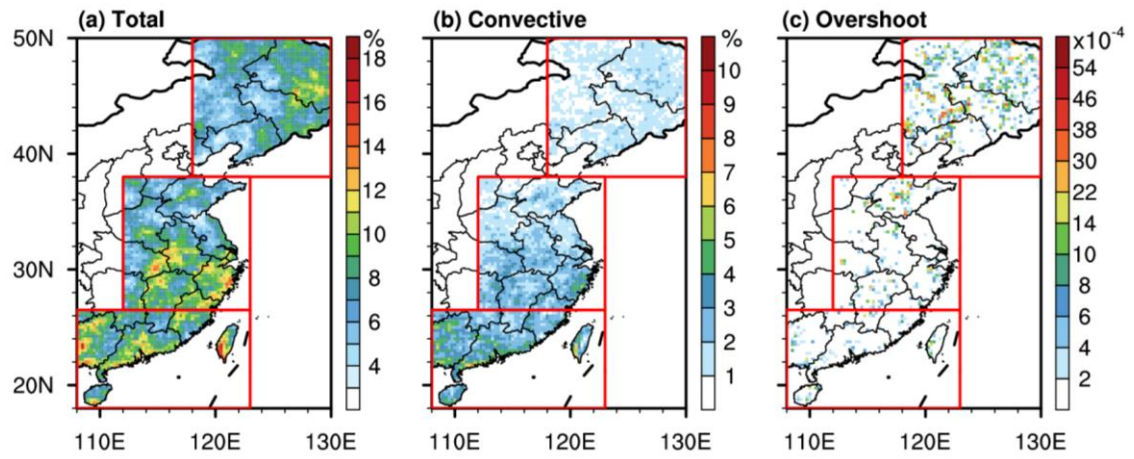
641

642 **Figure 4.** Geographical distribution of storm top height. **(a)** Distribution of storm top height for total precipitation.

643 **(b)** Distribution of storm top height for convective precipitation. **(c)** Distribution of storm top height for convective

644 overshooting.

645

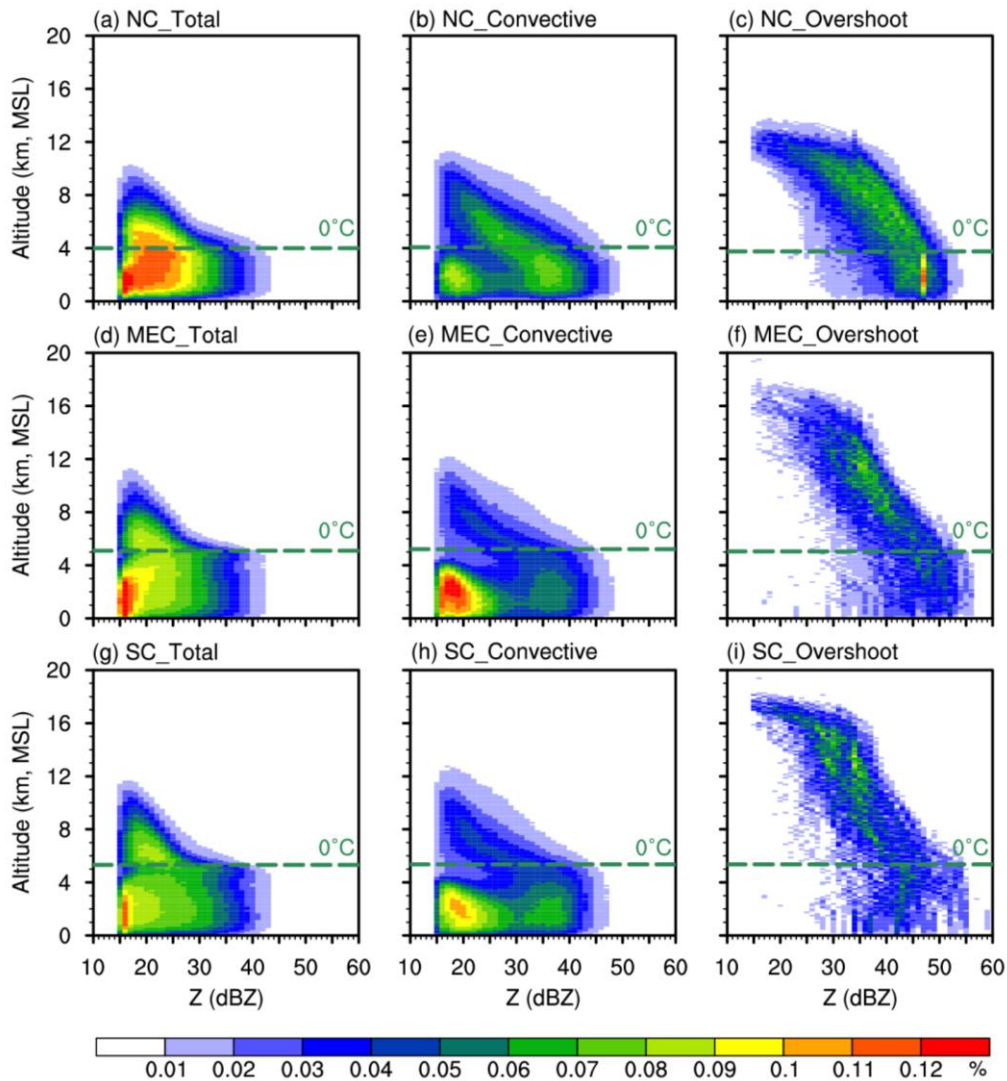


646

647 **Figure 5.** Precipitation frequency. (a) Frequency of total precipitation. (b) Frequency of convective precipitation.

648 (c) Frequency of convective overshooting.

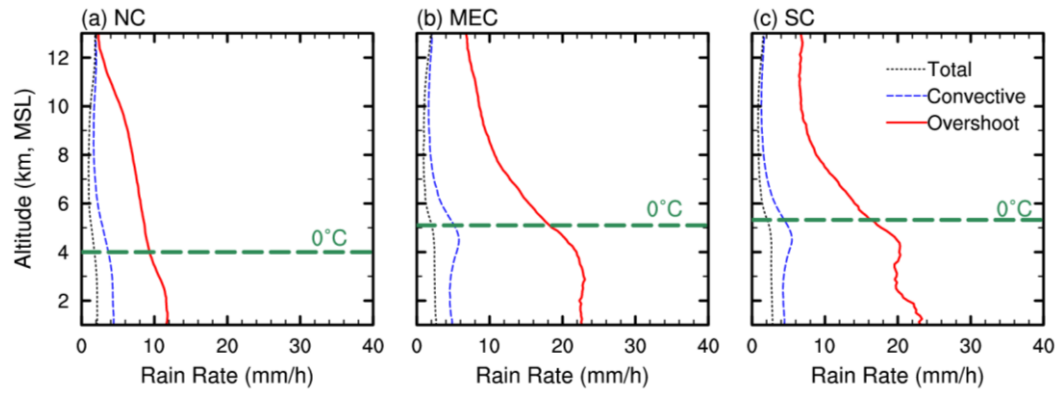
649



650

651 **Figure 6.** Contoured Frequency by Altitude Diagrams (CFADs) of radar reflectivity. (a) CFADs for total
 652 precipitation over NC (Green dotted line indicates the altitude of the freezing level). (b) CFADs for convective
 653 precipitation over NC. (c) CFADs for convective overshooting over NC. (d) CFADs for total precipitation over
 654 MEC. (e) CFADs for convective precipitation over MEC. (f) CFADs for convective overshooting over MEC. (g)
 655 CFADs for total precipitation over SC. (h) CFADs for convective precipitation over SC. (i) CFADs for convective
 656 overshooting over SC.

657



658

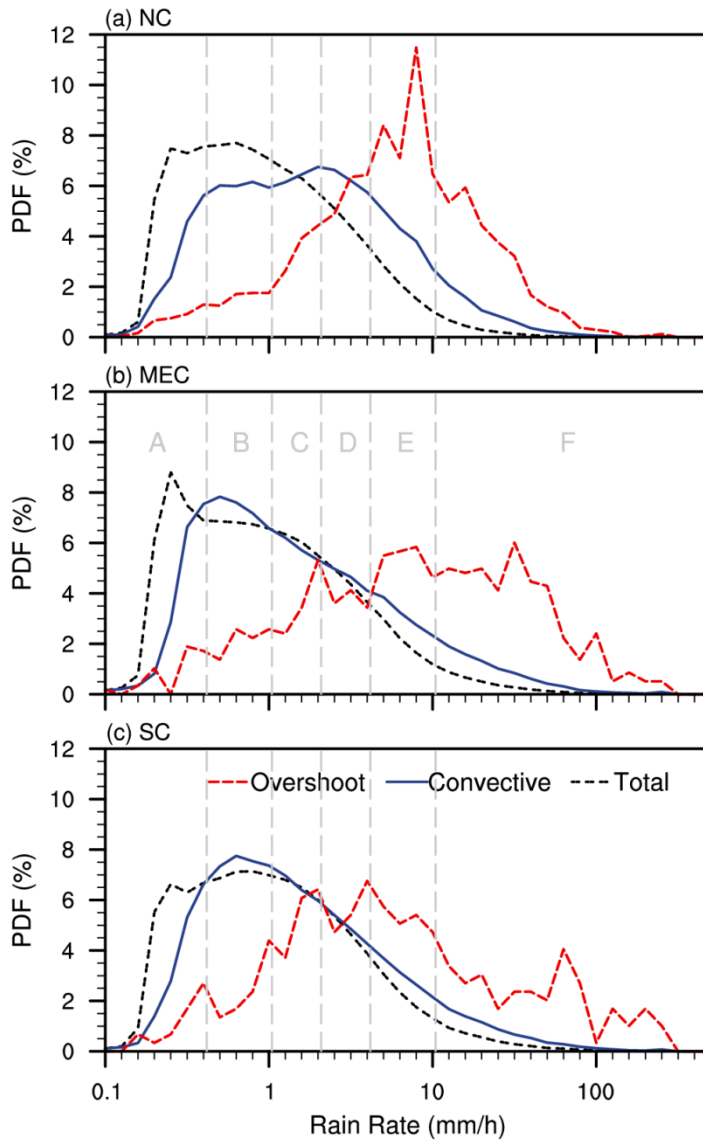
659 **Figure 7.** Rain rate profiles for total precipitation, convective precipitation and convective overshooting (Red lines

660 are convective overshooting; Blue lines are the convective precipitation; Black lines are the total precipitation). (a)

661 The rain rate profiles over NC (Green dotted line indicates the altitude of the freezing level). (b) The rain rate

662 profiles over MEC. (c) The rain rate profiles over SC.

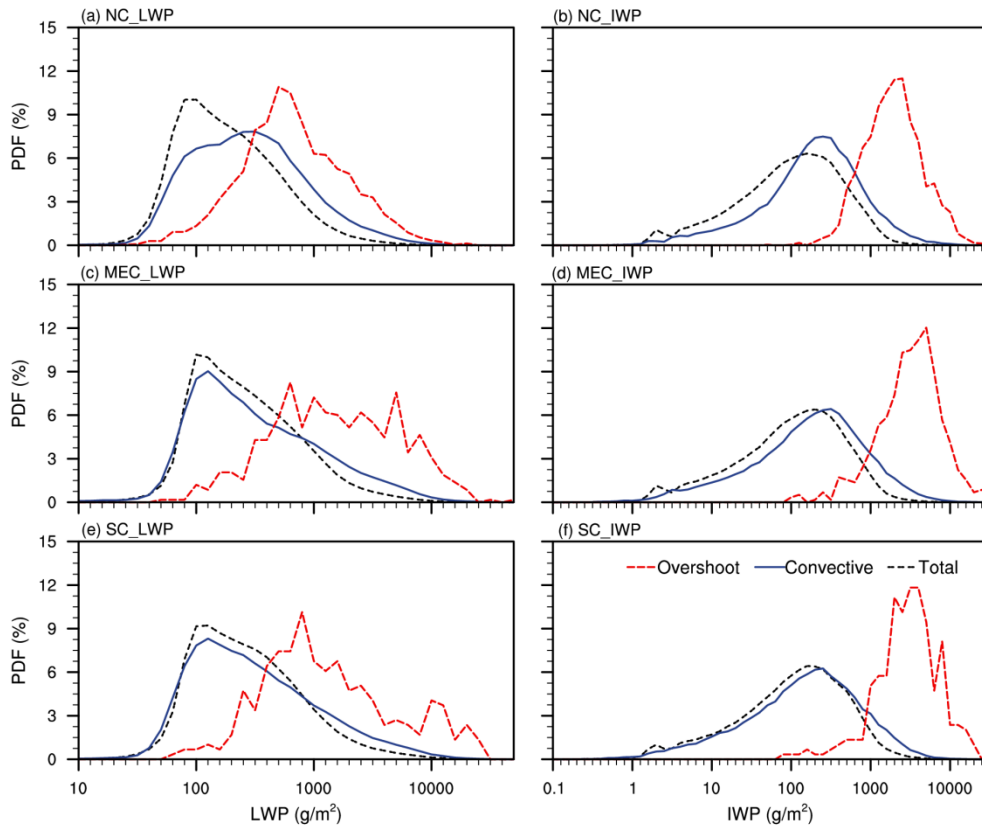
663



664

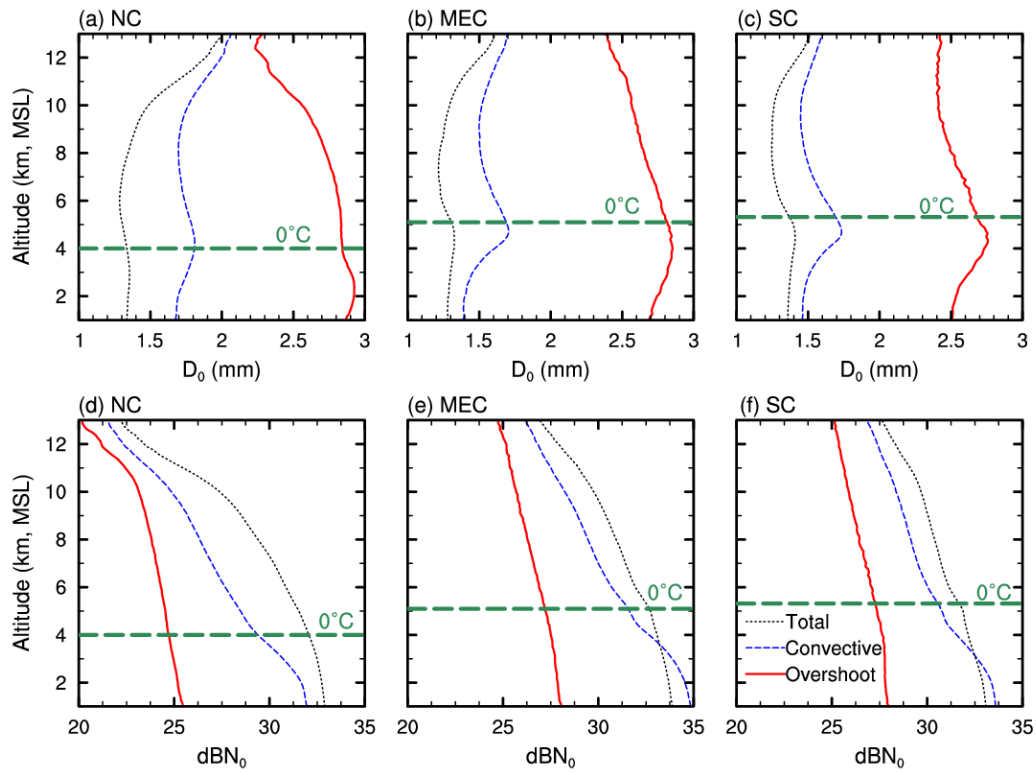
665 **Figure 8.** Probability Density Function (PDF) of Near Surface Rain Rate (NSRR). **(a)** PDF of NSRR in NC. **(b)**

666 PDF of NSRR in MEC. **(c)** PDF of NSRR in SC.



667
 668
 669
 670
 671

Figure 9. PDF of Liquid Water Path (LWP) and Ice Water Path (IWP). **(a)** PDF of LWP over NC. **(b)** PDF of IWP over NC. **(c)** PDF of LWP over MEC. **(d)** PDF of IWP over MEC. **(e)** PDF of LWP over SC. **(f)** PDF of IWP over SC.



672

673 **Figure 10.** The droplet concentration (dBN_0) and effective radius (D_0) profiles for total precipitation, convective
 674 precipitation and convective overshooting over NC, MEC and SC. **(a)** The dBN_0 profiles over NC (Green dotted
 675 line indicates the altitude of the freezing level). **(b)** The dBN_0 profiles over MEC. **(c)** The dBN_0 profiles over SC.
 676 **(d)** D_0 profiles over NC. **(e)** D_0 profiles over MEC. **(f)** D_0 profiles over SC.